Photothermal boiling in aqueous nanofluids

Edda T. Ulset[a], Pawel Kosinski[a], Yulia Zabednova[b], Oleg V. Zhdaneev[c], Pavel G. Struchalin[d], Boris V. Balakin[d,e,*]

[a] *Department of Physics and Technology, University of Bergen, Norway*
[b] *Department of Mathematics, University of Bergen, Norway*
[c] *Schlumberger, Russia*
[d] *NRNU Moscow Engineering Physics Institute, Norway*
[e] *Western Norway University of Applied Sciences*

Abstract

The process of photothermal evaporation in nanofluids finds promising applications in solar energetics, medicine and process technology. Previous studies report highly efficient production of solar steam in fluids with gold nanoparticles. In this article, we establish the process in nanofluids with less expensive carbon black (CB) and iron oxide (IO) nanoparticles (NP). Screening the concentration of nanoparticles, we tailor the nanofluids to reach the efficiency maxima: 66% at 3% wt (CBNP) and 75% at 10% wt (IONP); the steam was superheated up to 10 K (CBNP) and 16 K (IONP). It was also discovered that the IONPs-generated steam was contaminated with nanoparticles. In addition to experimental results, we have developed an empirical model of photothermal steam generation in nanofluids. The model agrees well with the experiments.

Keywords: solar steam, nanofluid, boiling, carbon black, iron oxide

1. Introduction

When nanofluid (NF) (i.e. fluid with suspended nanoparticles) is exposed to thermal radiation, the nanoparticles (NPs) effectively absorb the heat and transmit it into the surrounding fluid. In this case the inter-phase heat transfer becomes intensive because the integral nanoparticle-fluid contact area is sufficiently greater (by at least two orders) than in a traditional solar collector, where a continuous surface absorbs the sunlight. The microscale convection around the NPs and surface plasmon resonance at metallic NPs additionally intensifies the heat transfer. The nanofluids are thus used as coolants in modern direct absorption solar collectors (DASC). Otanicar et al. [1] reported enhancement of the collector efficiency by ∼7% when 0.25% wt of 20-nm silver NPs was dispersed in water in comparison with a "black surface" absorber. Karami et al. [2] succeeded in improving the photothermal performance of their solar collector by 25% using 20-nm copper oxide NPs at 0.01% wt.

*corresponding author, Boris.Balakin@hvl.no

According to the most recent experimental observations and theoretical estimates [3, 4], DASCs accumulate heat most effectively at around 0.50% wt NPs.

Although the nanofluid-assisted DASC technology is presently under evolutionary development aiming at a better stability of the nanofluids and screening new types of NPs, this method is rather well established. Nevertheless, another DASC application of the nanofluids that is attracting increased interest and is presently less well-known is the process of solar steam generation. Here the nanoparticles heat the carrier fluid up to saturation and generate steam that potentially can be used in micro-CHP systems, solar distillation and desalination. Other potential applications of the process include nanography, target cancer therapy, solar pond technology and selective evaporation.

The first experimental record on *in-situ* photothermal evaporation of nanofluid came from the Rice University [5]. By placing an aqueous suspension of 120-170 nm SiO_2 NPs, covered with gold shells, under the concentrated sunlight (> X100), the authors initiated subcooled boiling of the nanofluid with ∼82% efficiency. A subsequent experimental work published by the same research group [6] reports a pilot industrial test of the process. The transparent photothermal reactor with the nanofluid (NP number density $\sim 10^{10}$ m^{-3}) was located in the focus of the solar dish collector. The solar steam produced in the reactor was used for sterilization of waste by superheating up to 35 K, i.e. this steam could be used to drive a turbine. This concept was also adopted for the process of nanoparticle-driven photo-distillation [7] and off-grid bioethanol production [8].

Although the developed technology was found efficient at the laboratory scale, there are concerns that might complicate its industrial application. The main problem is the use of gold NPs, which are currently 250 times more expensive than the most frequently applied in "solar" nanofluids carbon black nanoparticles [9]. The degree of the nanofluid stability is unknown as the supplementary videos of the experiments [6] demonstrated intensive settling of the nanoparticles in the reactor. The toxicity of the steam due to the presence of Au NPs was not inspected. The theoretical background of the process is also unclear. Neumann et al. [5] assumed that the steam nucleation took place just on the surface of nanoparticles. This was not, however, confirmed in other works [10, 11] since heterogeneous nucleation at the nanoscale requires enormous superheat to exceed the Laplace pressure of the nanometric vapour shell. Finally, Neumann et al. [5] did not report the optimum concentration of the nanoparticles. An interesting experiment was conducted by Jin et al. [10] from Beihang University. In their study the solar steam was produced at natural irradiation, concentrated with Fresnel lens to 220 sun. Here an electrolyte with up to 13 ppm of 20-nm Au particles demonstrated efficiency of the order similar to the one detected by Neumann et al. [5]; a notable superheat of the steam was not registered.

A number of experimental works, inspired by Neumann et al. [5] were conducted under artificial illumination. The study of Ni et al. [4] (MIT) documented evaporation of the carbon black nanofluid in solar simulator. Nevertheless, the radiant heat flux (10 sun maximum) and the concentration of nanoparticles were not sufficient to superheat the steam; the maximum process efficiency of 60% was lower than in the aforementioned cases with natural irradiation of gold nanoparticles. Similar to this experiment, Wang et al. [12] documented evaporation of the nanofluid, composed of 500-nm carbon black nanotubes at artificial radiation of 10 sun.

The maximum NP concentration (0.002% wt), however, was not enough to boil the nanofluid because the steam was generated due to evaporation from the air-nanofluid interface at 50°C and the maximum evaporation efficiency was ∼48%. The nanofluids, composed of plasmonic nanoparticles, were evaporated under artificial illumination by Rahman et al. [13] (200-nm SiO_2-Ag NPs), Wang et al. [14] (10-nm Au NPs), Fu et al. [15] (50-nm Au at ∼2-μm graphene oxide NPs), Guo et al. [16] (up to 40-nm Au NPs) and Li et al. [17] (20-nm Ag at TiO_2 NPs) with evaporation efficiency that never exceeded 65% and with no superheating of the "luminate" steam. The last contribution in the list [17] reported contamination of the steam with nanoparticles; this aspect was not considered in other works. It is important to note that there are several studies that have focused on an alternative solution, which suggests evaporation of the fluid by focusing the sunlight at a sponge-like floating object with nano-pores. In this application the liquid, flowing into the pores due to capillary forces, evaporates in a slightly different way [18, 19]. Although this technique results in the equivalent evaporation efficiency (∼80%), the application might be sensitive to the purity of the utilized liquid as the existence of salinity gradients can lead to plugging of the pores [20].

From the provided literature survey, we conclude that the following issues remain unclear: (i) the composition of the nanofluid that results with the most efficient steam generation; (ii) the degree of the solar steam contamination with nanoparticles; (iii) a theoretical description of the process. The present contribution comes with a multi-factor examination of two different nanofluids from the photothermal evaporation point of view. Looking for a cost-effective solution, we produced nanofluids by use of tap water and widely available commercial nanopowders: carbon black (CB) and iron oxide (IO). At first, we aimed to define the optimum NP concentration of the nanofluids, focusing on superheat and efficiency of the process. Next, we condensed the generated steam and inspected NP-contamination of the condensate. Finally, we modified an existing theory of photothermal boiling to connect the kinetics of steam generation to the granulometry of the nanofluid and to reproduce the experimental results theoretically.

2. Experiments

2.1. Nanofluids

The nanofluids were produced dispersing nanopowders in tap water using the ultrasound bath Branson 3510 (320 W). The carbon black nanopowder (Timcal Ensaco 350G) with particle density 2250 kg/m^3, inspected with JEOL 2100 transmission electron microscope (TEM), revealed the average individual particle sizes 51±17 nm. The dry nanoparticles of iron oxide (Fe_3O_4) with density 5240 kg/m^3 and particle size 184±55 nm were purchased from SigmaAldrich. The sizes were defined based on their projected area that was measured in ImageJ after bandpass and watershed filtering. The particle size distribution, shown in Fig. 1, was uni-modal and normal-like for both nanoparticle types. The chemical composition of the tap water from Bergen communal network (pH 8.2) is presented in the supplementary materials (Table. S.0). The dry nanoparticles (see Fig. 2 (right)) were dispersed in water without surfactants, which resulted in partial agglomeration in both nanofluid types. This is

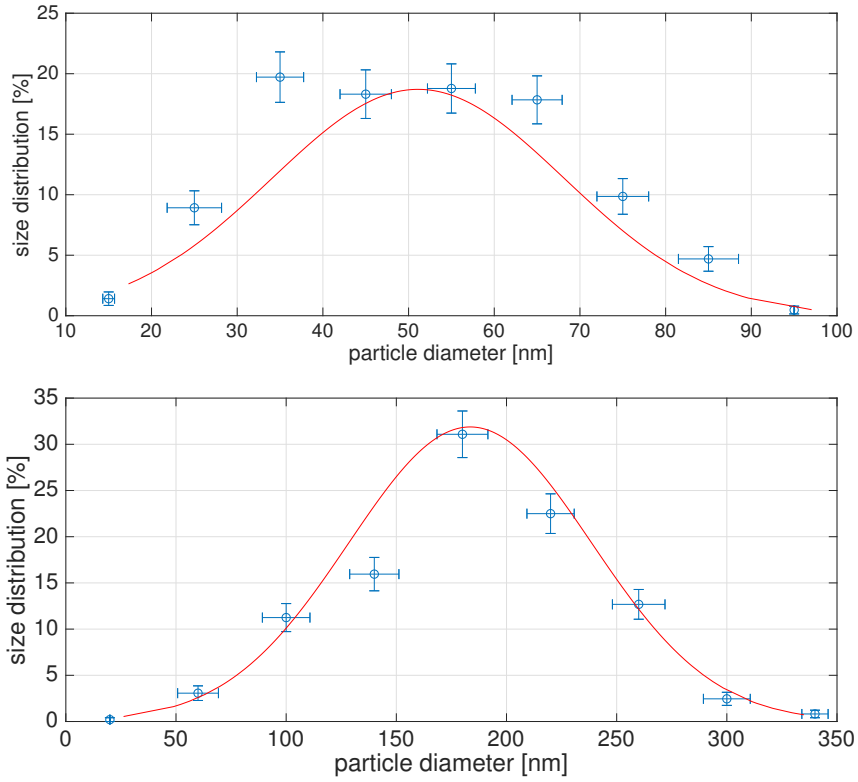

Figure 1: Particle size distribution function for dry CB (top) and IO (bottom) nanoparticles

also identified through optical inspection of CBNF (Keyence DM VHX 2000); the nanoparticles agglomerated up to the maximum sizes ∼7 μm (the micro-photography of CBNF is shown in Fig. S.1). The larger and heavier IONPs with lower Hamaker constant [21] agglomerated with a lower intensity at equivalent experimental conditions. Although agglomeration of nanoparticles was detected in both nanofluids, the samples were kinetically stable during the process of the photothermal boiling due to the Brownian motion and due to the fact that the velocity of thermal convection ∼0.07 m/s (this number is discussed later in the paper) exceeded the NP settling velocity of $3.3{\cdot}10^{-5}$ m/s (St<<1).

2.2. Photothermal experiments

The experimental set-up, schematically illustrated in Fig. 2 (left), consisted of: a cylindrical glass tube (ID 13.5 mm, height 148 mm), sealed from the top with a rubber plug; two halogen lamps OSRAM (Haloline 230 V 400 W), radiating at the glass tube; a 200-ml cylindrical condensate collector and a spiral, flexible PVC piping (ID 3 mm, length 48 cm) which was connected the glass tube to the collector. The steam, produced in the glass tube, was completely condensed in the PVC-pipe due to the natural convection of the surrounding air at ambient conditions (23-25°C, 1 bar).

The two lamps were placed perpendicularly (Fig. 2) in order to prevent mutual heating

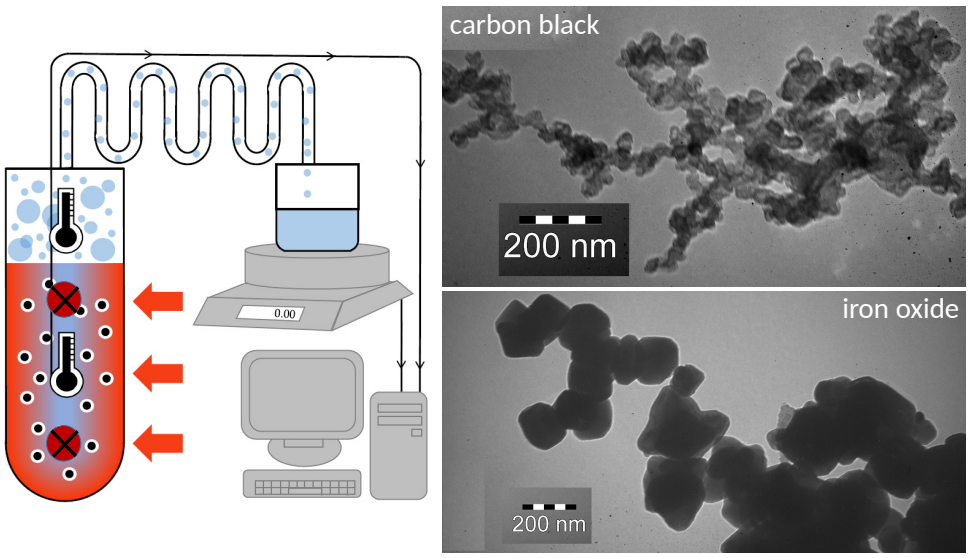

Figure 2: Schematic description of experiments (left), TEM images of NPs (right)

of the lamps. The glass tube was located at the 10-cm distance from each lamp, corresponding to the radiate heat flux of 5760 W/m^2 from a single lamp. The sample was positioned outside the convective zone, which was formed in the air around the lamps [22]. The thermal radiation intensity from a single lamp at different distances along the light-path was measured with LS122 radiometer from Aermanda. The radiometer was calibrated in-house using Sol3A Class AAA Solar Simulator from AZPECT. This information is provided in the supplementary material (Fig. S.2). The electromagnetic spectrum of the lamps, determined by the use of Ramses AAC-VIS radiometer (±0.2 nm, TriOS), was shifted ∼350 nm to the red zone relative to the solar spectrum; this was also confirmed by OSRAM [23].

The measurement system included two T-type thermocouples from Omega (±0.3°), located along the centreline of the glass tube at 2.2 and 13.1 cm from the top in order to continuously immerse the sensors into the steam and the fluid phase. The first sensor (located in the steam) was placed outside the irradiated zone. The distance between the lamps and the second sensor (∼ 10.7 cm) was greater than the optical depth of the nanofluids. The measurement was thereby not significantly influenced by thermal radiation of the lamps. The condensate collection rate was registered with the precision scale Sartorius CPA 324S (±0.1 mg). The scale and the thermocouples (via the digital transmitter) were connected to a PC, recording the measurement every second. During the experiments we altered mass fraction of CBNPs and IONPs in a 5-ml nanofluid sample up to 10% wt. Higher concentrations are not considered in the present paper since the nanofluids became unstable and formed a stationary viscous bed at the bottom of the sample above this limit. The evaporation of each sample was performed for 30 minutes. The presence of nanoparticles in the condensate, collected after each run, was inspected by means of Raman spectrometry (RamanRxn1 Analyzer) and static light scattering (Fritsch Analysette 22).

3. Results and discussion

Boiling of both nanofluids started after a short heating period (∼7 min, a similar heating time was reported by [4]), during which the nanofluid temperature rose from the ambient temperature up to the saturation conditions (see Figs. S.3.1-S.3.2) almost independently on particle concentration. After this point, IONF temperature became constant until the end of each irradiation session. For this nanofluid, no steam with significant superheat was produced in the bulk of the fluid. CBNF nanofluid boiled at low superheat values (2-3 K) for the samples with concentration below 1%. CBNF temperature for higher concentrations did not differ from IONF.

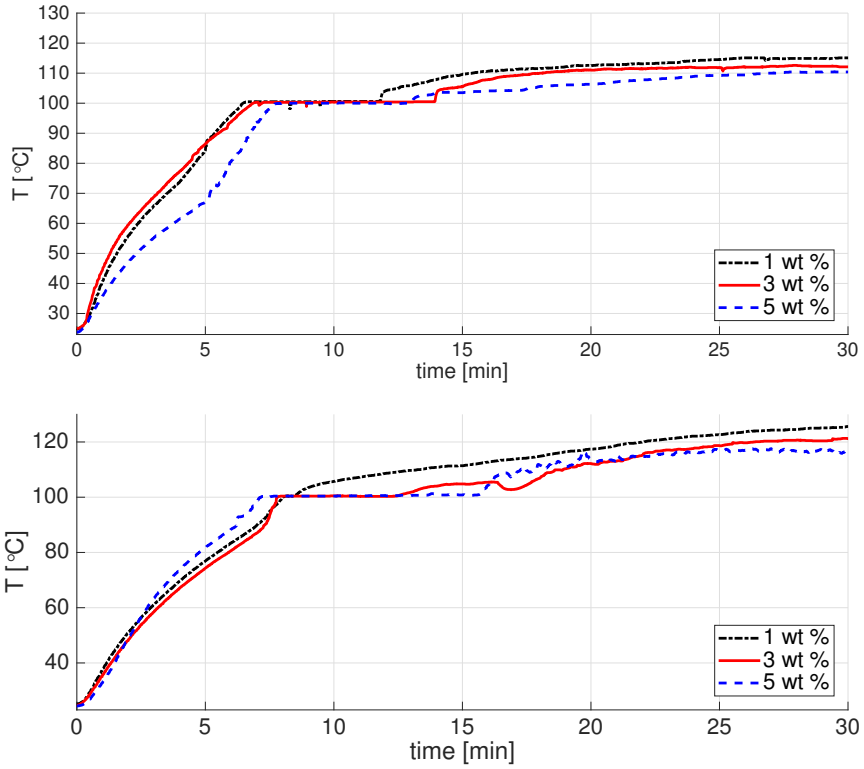

Figure 3: Temporal history of steam temperature for CBNF (top) and IONF (bottom) at particle concentrations 1%, 3% and 5%.

The temperature, detected by the steam sensor, is shown in Fig. 3 for both nanofluids. At the initial steps of the process CBNF steam temperature did not deviate significantly from the nanofluid temperature. After the saturation conditions are established, the temperature remains at saturation until ∼20% of the sample has evaporated. IONF did not exhibit any sufficient temporal delay in saturation at particle fractions below 2% wt, even though it demonstrated behaviour similar to CBNF at larger concentrations. The magnitude of the superheat was almost twice greater for IONF steam. This is demonstrated in the figure and Table 1, which shows time-average superheat for both nanofluids at different concentrations.

Table 1: Time-average superheat ΔT (K) for different NP concentration

concentration [% wt]	0.3	0.5	1.0	2.0	3.0	4.0	5.0	10.0
CBNF	5.0	7.4	9.5	8.3	6.0	6.2	6.9	6.7
IONF	13.1	14.4	15.8	13.6	10.1	6.1	9.1	11.3

CBNF steam increases superheating with a concentration up to the maximum of 9.5 K at 1%. Further, reduction of superheat is weakly dependent on concentration. To our knowledge, there has been no equivalent superheat detected in previous studies of CBNF under external radiation. Moreover, these values exceeded 6.5 K that corresponds to conventional water boiling curve at 5760 W/m^2 [24] from a heating surface under normal conditions. According to our supplementary computational fluid dynamics (CFD) analysis, performed for the steam flow in the experimental set-up (Fig. S.4), the steam pressure was negligibly over 1 bar so that the superheat cannot be explained by over-pressurization. The superheat of IONF steam is dependent on the nanoparticle concentration in an equivalent way, having a maximum of 15.8 K at 1%. Amjad et al. [25] and Neumann et al. [5, 6] observed similar values of superheat for the Au-water system heated with $\sim$ 200 sun.

Figure 4 presents evaporation kinetics for both nanofluids. Both nanofluids produced steam with the mass flow of similar magnitude, clearly demonstrating of an optimum concentration between 1% wt and 5% wt, above which the evaporation drops down. When considering these results, it is possible to denote two opposite drivers that define qualitative behaviour of the steam temperature: more intensive trapping of the nanoparticle thermal boundary layers (Ni et al. [4]) due to evaporation (and respective densification of the particulate phase) is responsible for increasing superheat with time; the reduction of superheat with particle concentration is caused by more intensive absorption of the light at the boundaries of the experimental system and so limited exposure of the bulk. Taking into account density and size difference between CBNPs and IONPs, it is important to note that IONF generates steam more effectively even with a lower number of particles. This could be attributed to multiple differences between the mentioned nanofluids: IONF is of higher thermal conductivity [26] and is better exposed by thermal radiation in the bulk; IONPs are hydrophylic and surface plasmon resonance takes place at the IONPs. Moreover, the difference in the nanofluid granulometry that influences boiling kinetics must be taken into account and is discussed in the following section.

3.1. Efficiencies

Another crucial technical parameter that describes the overall thermal performance of the considered system is process efficiency. Here, depending on application, two possible cases were considered. The heat absorption efficiency, which is important if the nanofluid is planned to be exploited in a direct absorption solar collector without boiling:

$$\eta_a = \frac{\int_{T_0}^{T_1} m\, C_{NF}\, dT}{\int_{t_0}^{t_1} \overline{q} A\, dt}, \tag{1}$$

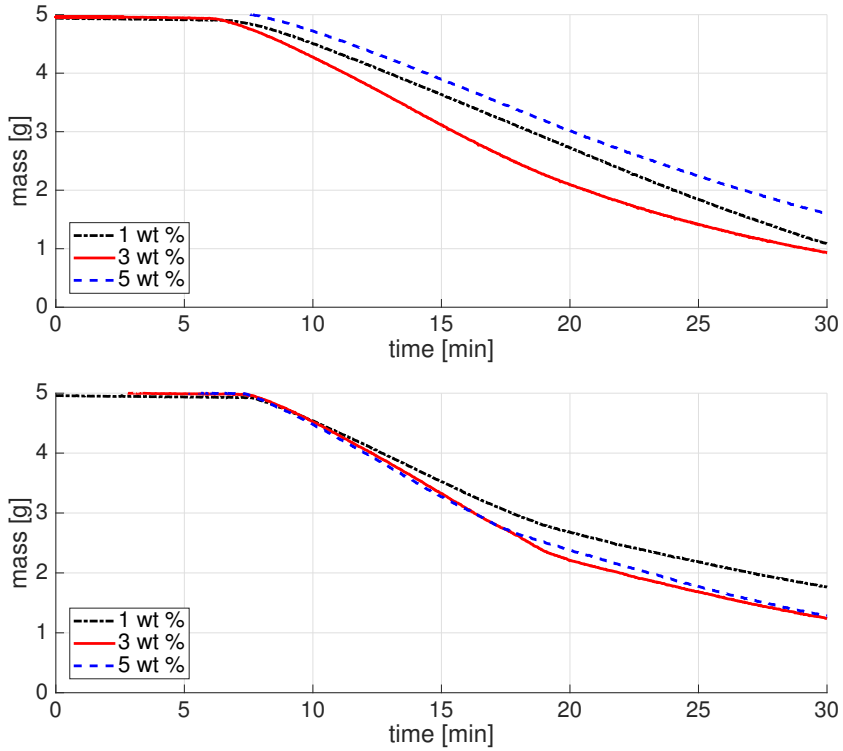

Figure 4: Mass of the sample as a function of time for CBNF (top) and IONF (bottom) at particle concentrations 1%, 3% and 5%.

where C_{NF} is the specific heat, m is the mass of the nanofluid and A is the irradiated area of the collector; these variables are time-dependent. Equation (1) is to be integrated from the start of the experiment, $t = t_0$, until the boiling point has been reached at the time t_1. This corresponds to the initial temperature at T_0 and the saturation temperature T_s. The specific heat C_{NF} is estimated assuming homogeneous mixture of the fluid and the nanoparticles, scaling the respective parameters of each phase with the time-specific mass fraction of the nanoparticles f_{NP}: $C_{NF} = C_l\,(1 - f_{NP}) + C_{NP} f_{NP}$ (indices NP and l denote the nanoparticles and the base liquid). The average heat flux from the lamps $\overline{q}$ is defined as $\overline{q} = (2/D) \cdot \int_0^D q(z)dz$, where z is the direction of lamp light, D is the internal diameter of the experimental tube (Fig. 2) and $q(z)$ is a fitted function of experimental measurement (see Fig. S.1).

The time-average absorption efficiency for our experimental system is plotted against concentration in Fig. 5. It follows from the figure that the efficiency was always above 55.0%, increasing with the particle conncentration up to 66.7% at the optimum concentration of 1% wt for CBNF. This concentration was twice greater than the one reported in [3] and [4] as the optimum of photothermal absorption. After this point the efficiency starts to decay with CBNPs concentration, while the photothermal performance of IONF increases continuously with concentration up to 84.2%. The qualitative dependence of absorption efficiency on

particle concentration is equivalent to the one discussed for superheat (Table 1). There is however an alternative explanation for the existence optimum concentration by Mynkowycz et al. [26], who suggested that the most intensive natural convection established in the nanofluid with the maximum achievable effective thermal conductivity and the minimum possible effective viscosity. Both parameters, being proportional to the concentration of nanoparticles, rich equilibrium at volume fractions which correspond to 2-5% wt. These values differ from the optimum, detected in our study.

It is interesting to compare the photothermal performance of our system to the results reported in other relevant works, which are also shown in Fig. 5. Here we conclude that a number of different nanofluids exhibited similar photothermal performance, increasing the efficiency up to the optimum f_{NP} <1% and slightly reducing the photothermal performance above this concentration. Considering points (3) and (4) from Fig. 5 for Ag nanofluid of the same concentration but different particle size [1], it is possible to conclude that the photothermal performance is inversely proportional to the size of the nanoparticles. The absorption efficiency of most of the third-party systems was however, slightly lower than in our case even though much smaller nanoparticles were used (up to 50 nm). This observation may be explained by the absence of fully developed natural convection of the nanofluid during the experiment. Indeed, a major part of these systems were heated by a lower radiative heat flux (typically 1 sun), coming from the top of the solar collector, i.e. the convective currents of expectantly lower magnitude could establish there only due to sedimentation and thermophoresis of nanoparticles. Moreover, as it follows from point (2) in the figure, the photothermal performance of the system does not sufficiently improve when the radiative heat flux approached our values (10 sun) while still being directed along the direction of gravity. The importance of convective mass transfer in the bulk of the fluid is further illustrated by point (1) where the recirculating solar collector system was considered. Here the nanofluid was mixed due to the forced convection that resulted with the absorption efficiency well above 80% at the mass concentration of nanoparticles below 0.1%.

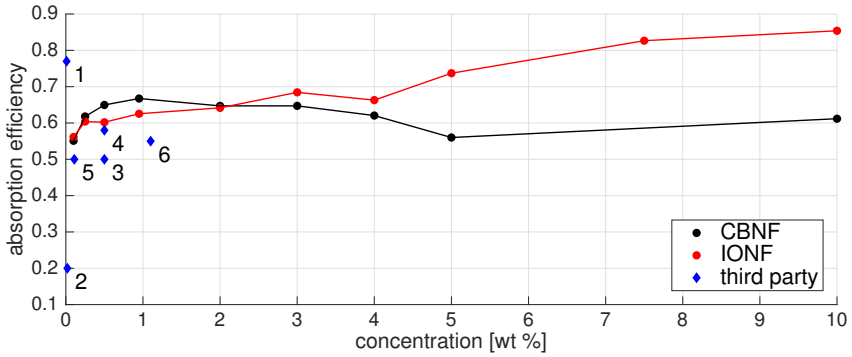

Figure 5: Time-average absorption efficiency as a function of nanoparticle concentration for CBNF and IONF. Third-party data: 1 - 40 nm CuO, 1 sun (Karami et al. [2]); 2 - 10 nm Au, 10 sun (Wang et al. [14]); 3 - 40 nm Ag, 1 sun; 4 - 20 nm Ag, 1 sun; 5..6 - 30 nm graphite, 1 sun (Otanicar et al. [1]).

Furthermore, we considered the evaporation efficiency that defines the amount of heat necessary to generate and superheat the steam as shown in Fig. 4:

$$\eta_e = \frac{\int_{m_1}^{m_2} (r_{lv} + C_v \Delta T) dm}{\int_{t_1}^{t_2} \overline{q} A \, dt}, \tag{2}$$

where m alters over the mass of the vapour produced when boiling commences from the initial mass m_1 to the final mass m_2, r_{lv} is the latent heat of vaporization, C_v is the specific heat of the steam and ΔT is the superheat.

The dependence of the time-average evaporation efficiency on the nanoparticle mass concentration is shown in Fig. 6. As it follows from the figure, η_e for the IONF varies with concentration in a way similar to η_a, increasing from 30% up to 75% at 10% wt. The slope of the dependence is, however, steeper that than that of η_a. The evaporation efficiency of CBNF is again proportional to the respective absorption efficiency, while the maximum of 65.9% shifts to 3% wt. Here it is possible to conclude that the steam generation optimum, compared with η_a, is more dependent on the concentration of particles in the system. The particles, and particularly their micro-sized agglomerates, act not only as the absorbers of the thermal radiation: their surface also constitutes a nucleation site for heterogeneous nucleation of steam bubbles. The evaporation efficiencies defined in third-party experiments on photothermal boiling of different nanofluids are also shown in Fig. 6. According to the data, our results exceed by about 20% relative to the cases where CBNFs (500 nm and 5000 nm) were studied at similar heat flux of 10 sun [14, 4], but directed along the gravity direction, i.e. cases with limited convection of the NF. The experiments, conducted with Au NPs exceeded our evaporation efficiency by 7-8% even in cases of lower solar concentration (1 sun) and again heated along the gravity direction. This is explained by much higher thermal absorption for gold NPs. To our knowledge, the absorption and evaporation efficiencies for mass concentrations above 2% were not considered in the literature.

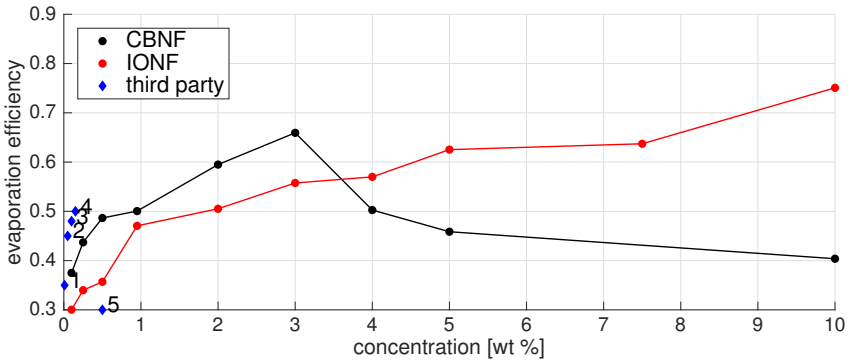

Figure 6: Time-average evaporation efficiency as a function of nanoparticle concentration for CBNF and IONF. Third-party data: 1 - 500 nm carbon nanotubes, 10 sun (Wang et al. [12]); 2,3,4 - 75 (l) x 18 (d) nm Au nanocylinders, 1 sun (Liu et al. [27]); 5 - 5000 nm CB [28], 10 sun (Ni et al. [4]).

3.2. Boiling kinetics

Making use of mass reduction curves from Fig. 4, it is possible to evaluate the volumetric flow of the steam produced in both nanofluids. The result is presented in Fig. 7 for different nanoparticle concentrations, where we also focus on concentrations not shown in Fig. 4. The flow rate exhibits complex non-monotonic behaviour, initially reducing at the lowest mass fraction down to a minimum of approximately 0.5%. This most probably occurs when the temperature probe, acting itself as a steam generation surface, becomes shielded by the nanoparticles, so that the evaporation driven solely by nanoparticles begins. The production rates further rise to maxima at 2%, 5% (CBNF) and 4% (IONF). We observed and described a similar behaviour of the efficiencies for CBNF in Figs. 5-6, although the volume flow rate demonstrates greater sensitivity to concentration. Comparison of production rates for CBNF and IONF should be performed taking into account the difference in density and particle size between the nanofluids as IONPs, <50 times outnumbered relative to CBNPs, and generating steam at just slightly lower rate.

As seen in Fig. 7 the average production rate for both nanofluids is ∼0.4 l/min at the effective absorption area $1.2{\cdot}10^{-3}$ m^2. This amount of steam could be potentially utilized in a nano-turbine application, for example QuasiTurbine [29] (2 kW type), which requires about 300 l/min. This would correspond to the production of steam out of our NFs in a solar concentrator with irradiated area up to 1 m^2. This generation would potentially result in ∼500 We without steam overpressure. Accounting for 11-fold magnification, which is equivalent to our experiments, the target steam generation rate requires up to 11 m^2 of solar concentrator, which is obviously a lowest estimate and does not account for possible thermal losses.

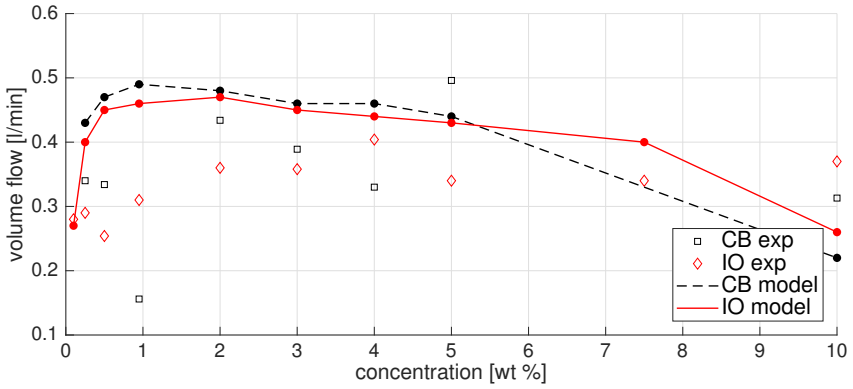

Figure 7: Steam production as a function of mass concentration. CBNF and IONF results are compared with Equation (6)

It is interesting to provide an order-of-magnitude estimate for the steam generation rate. This will furthermore depend on the nanofluid granulometry as the nanoparticles agglomerate when agitated in water due to thermal convection. This takes place at velocity $u = \sqrt{g\beta\Delta T_c H} \approx 0.07$ m/s, where ΔT_c is the maximum temperature difference along

the nanofluid column and H is the height of the boiling column. The nanoparticles cease to agglomerate when the adhesive van-der-Waals force, acting on agglomerate of size d_a, $F_a = Ad_a/24h_0^2$ [30], becomes counter-balanced by the force of viscous retardation from the fluid $F_d = 0.75\pi\mu d_a^2 v_r/h_0$ [31], where the inter-particle relative velocity is proportional to the shear rate $v_r \approx \gamma d_a$. Then the agglomerate size reads:

$$d_a = \sqrt{\frac{A}{18\pi\mu\gamma h_0}}, \tag{3}$$

where $A_{CB} = 4.5{\cdot}10^{-20}$ J [32] and $A_{IO} = 2.0{\cdot}10^{-20}$ J [21] are the nanoparticle Hamaker constants (calculated in water following [30]), $\gamma \approx 40$ s^{-1} is the shear rate (estimated using the aforementioned flow velocity and the inner diameter of the tube), $\mu = 0.9$ mPa·s is dynamic viscosity and $h_0 \approx 0.2$ nm is the cut-off distance [30]. Equation (3) returns $d_{a,CB} = 10.5$ μm and $d_{a,IO} = 7.0$ μm, being in satisfactory agreement with the results of optical microscopy (CBNP sample, Fig. S.2) where $d_{a,CB} \sim 7$ μm was detected.

Following Mikic et al. [33], we define the minimum superheat that is required to generate steam shells around the nanoparticle agglomerates:

$$\Delta T = \frac{4\sigma T_s}{\rho_v d_a r_{lv}}, \tag{4}$$

where $T_s = 373$ K is the saturation temperature, $\sigma = 60$ mN/m is the surface tension, $\rho_v = 0.59$ kg/m^3 is the steam density and $r_{lv} = 2.23{\cdot}10^6$ J/kg. Using particle sizes, calculated with Equation (3), we obtain $\Delta T_{CB} = 6.5$ K, $\Delta T_{IO} = 9.7$ K, which is again in agreement with the time-average experimental values from Table 1; estimation for IONF demonstrates greater discrepancies. The observed correspondence between the theoretical and the experimental superheat may probably support scenario of vapour shells formation, suggested by Neumann et al. [5].

Assuming the steam bubble was formed around the agglomerate of nanoparticles, we further proposed that the bubble expands, meets its neighbours from the other agglomerates and grows until its tip steps outside the hot boundary layer with most efficient absorption of radiated heat [34]. This is illustrated in Fig. (8) (left). The resulting steam bubble with the maximum size, shown schematically in Fig. 8 (right), is heated by a cloud of nanoparticles. The boundary layer is rather well approximated by the optical depth of the nanofluid $d_{b,\max} \sim K_{NF}^{-1}$. The extinction coefficient is estimated as $K_{NF} \approx K_l + 6\phi/d_a$ [35], where K_l is the average extinction coefficient of water and ϕ is the volume fraction of nanoparticles. Knowing the maximum size of the steam bubble, the heating directions (see Fig. 8) and geometry of the experimental system, it is possible to calculate the total volume of steam produced under the optical depth:

$$V_\Sigma = \frac{3\pi}{16}\left[2D \cdot d_{b,\max} - d_{b,\max}^2\right] \cdot H \cdot n_b \cdot V_{b,\max}, \tag{5}$$

where n_b is the number density of the steam bubbles, estimated as reciprocal of the maximum

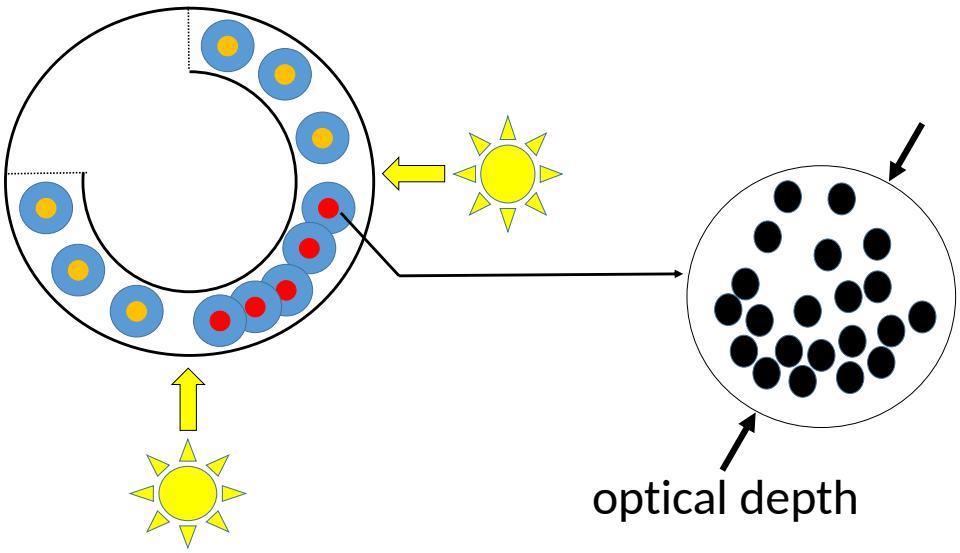

Figure 8: Schematic description of photothermal boiling. Steam bubbles incorporate nanoparticles. The hottest zone, irradiated with two lamps, is highlighted in red.

steam bubble volume $V_{b,\max}$. The volume flow rate of the produced steam then becomes:

$$Q \sim \frac{V_\Sigma}{\tau_g} \cdot \left(\frac{T_s}{T_s + \Delta T} \right) \cdot \left(\frac{p_a + 4 \cdot \sigma / d_{b,\max}}{p_a} \right), \tag{6}$$

where p_a is the ambient pressure and τ_g is the time, required for the bubble to grow from d_a to $d_{b,\max}$. The latter can be found making use of the technique, developed by Dietzel and Pulikakos [36] for the process of radiative evaporation in nanoinks:

$$\begin{aligned} 3/4 \cdot \overline{q} \cdot A_{NP,b} \cdot \tau_g \sim \left(\rho_{NP} V_{NP,b} C_{NP} + \rho_v \left[V_{b,\max} - V_{NP,b}\right] C_l\right) \Delta T + \rho_v \cdot \left[V_{b,\max} - V_{NP,b}\right] \cdot r_{lv} \\ + \sigma \left(A_{b,\max} + A_{NP,b} \cdot \cos\chi - 4 \cdot V_{b,\max}/d_{b,\max}\right), \end{aligned} \tag{7}$$

where index v denotes the vapour; $A_{b,\max}$, $V_{b,\max}$, are the surface area and the volume of the maximum bubble and χ is the wetting angle. Surface area $A_{NP,b}$ and volume $V_{NP,b}$ of the nanoparticles residing inside the maximum bubble, is proportional to the respective parameters of a single nanoparticle agglomerate d_a, increased by the total number of particles in the maximum bubble $\phi \left(d_{b,\max}/d_a\right)^3$. Equation (7) balances the total thermal energy, harvested by the particles (left-hand-side) with the amount of heat spent to: superheat the nanoparticles and corresponding to $d_{b,\max}$ mass of the fluid (1^{st} therm in the right-hand-side), evaporate the fluid (2^{nd} term) and form the liquid-steam inter-phase (3^d term).

Making use of the technique proposed in Eqs. (3-7), we estimated the volumetric flow rate, also accounting for wettability of the nanoparticle surface. For hydrophobic CBNPs the wetting angle was selected to be $\chi_{CB} \sim 3\pi/4$, and for hydrophilic IONPs $\gamma_{IO} = 0$. The calculation results of the model are shown in Fig. (7) for different concentrations of nanoparticles. The theory agrees well with the experimental results both qualitatively and

quantitatively, exhibiting two maxima at 1% and 2% for CBNF and IONF respectively. The most important discrepancies are apparently observed in the region of low concentrations, clearly demonstrating the effect of steam generation at the sensor probe. The calculation slightly overestimates the experimental results because the model does not account for a temporal delay due to nucleation of the primary steam bubble. Moreover, the surface plasmon resonance was not considered for IONF. It is interesting to note that the bubble growth time τ_g ($\sim$ 10-30 ms) was of the same order as the average time, required for the nanoparticles to settle in the steam bubble of $d_{b,\max}$, that was calculated assuming the Stokesian settling of the nanoparticles. Most of the nanoparticles were therefore located at the bottom of the maximum bubble. Taking into account density difference for CBNPs and IONPs, it is possible to assume the steam bubbles of IONF were less mechanically stable.

3.3. Condensate

The Raman spectra of the solar steam condensate are presented in Fig. 9 for CBNF (top) and IONF (bottom). The samples of CBNF condensate did not display signs of contamination by CBNPs when compared with a reference sample of nanoparticle-free water. Here we did not observe peaks at the D-band (1340 cm^{-1}) and the G-band (1580 cm^{-1}) [37], which are common for CB. In addition, the condensate was visually free from the NPs. The IONF condensate, evaporated from the nanofluid samples with concentrations below 5% wt, did not demonstrate clear signs of contamination of IONPs even though IO presence was observed visually in the condensate samples. However, we did find the peak, associated with Fe(III)-O at 686 cm^{-1} [37] for IONF samples with higher concentration.

The results of the static light scattering analysis (SLS) are shown in Fig. 10 for the condensate, obtained from two similar NP volume fraction samples of CBNF (4.7%) and IONF (4.6%) in terms of the particle size distribution (PSD) function. The SLS data from a reference sample of clean water is given in the supplementary materials (Fig. S.5). Superimposing both PSDs against the reference water sample, it was found that the CBNF condensate sample had similar characteristics to water, having two maxima with particle sizes at 500-700 nm and 4-6 μm which can correspond to natural contaminants and air bubbles. The IONF condensate sample exhibits another peak of much smaller particles up to 300 nm that are evidently IONPs.

It is possible to estimate the size of the heaviest nanoparticle, that is lifted by the flow of steam and therefore capable of escaping the experimental system. Balancing the drag force, acting on the particle from the steam with gravity, and neglecting other forces, we obtain:

$$d_{NP} \sim \frac{3}{4}\frac{C_D \rho_v u^2}{\rho_{NP} g}, \tag{8}$$

where the drag coefficient $C_D \sim 0.42$ and mean steam velocity is derived from the experimental volume flow $u = 4Q_{exp}/\pi D^2$. Equation (8) returns d_{NP} <100 nm for both CBNF and IONF, which is at least of the same order for IONPs but is much lower than the values, detected from SLS for CBNPs. We attribute this observation to different wettabilities of the carbon black nanoparticles, which were most probably captured by the nanofluid-steam interphase.

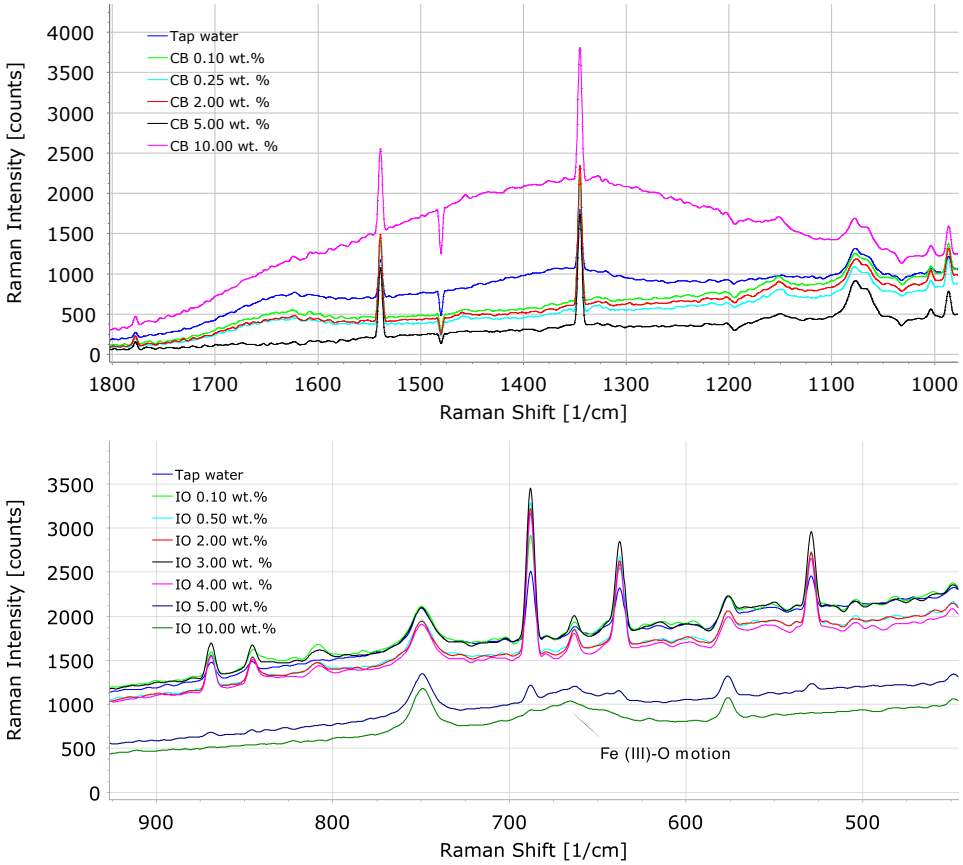

Figure 9: Raman spectrum of condensate from CBNF (top) and IONF (bottom).

4. Conclusions

This paper reports experimental results on the photothermal boiling of two different aqueous nanofluids, produced with carbon black and iron oxide nanoparticles. The "luminate" steam, generated in the fluids by the use of artificial radiation, was superheated stronger (up to 15.8 K) than this would be expected for the conventional heating of water at the experimental heat flux. By taking a closer look at the granulometry of the produced nanofluids, we were able to provide an order-of-magnitude theoretical estimate of the superheat observed.

The iron oxide nanofluid demonstrated better thermal performance than the carbon black nanofluid, continuously increasing efficiency of the process with mass concentration (up to 75% at 10% wt) and more intense superheating the steam. The optimum concentration of 3% wt, on contrary, was detected for the carbon black nanofluid, with the maximum efficiency of 66%. Inspecting condensate of the "luminate" steam, we observed significant amount of the iron oxide nanoparticles, which makes this nanofluid less attractive from the environmental viewpoint. The condensate from the carbon black nanofluid was free of the nanoparticles.

Adopting a simplistic heat balance method from the literature, it was possible to replicate steam production rate theoretically. Our model, which was based on the theoretical work by Dietzel and Poulikakos [36], demonstrated modest discrepancies relative to the experiment. We have also analysed the kinetics of steam generation, upscaling the process for a potential use in a solar generator system for micro-CHP (up to 500 kWe). Following our estimates, the technology potentially becomes competitive with the photo-voltaic when an organic base fluid with lower latent heat is used instead of water.

Acknowledgements

This study was supported by Russian Science Foundation (project 17-79-10481). We would like to thank Dr. K. Redkin (WHEMCO Inc.), Prof. C.I. Garcia (University of Pittsburgh) and Dr. D.P. Shornikov (NRNU Moscow Engineering Physics Institute) for their help with granulometric characterization of nanofluid samples; Dr. S.V. Boriskina (Massachusetts Institute of Technology) and Prof. K.V. Kutsenko (NRNU Moscow Engineering Physics Institute) for useful discussions when we conducted this study.

References

[1] T. Otanicar, P. Phelan, R. S. Prasher, G. Rosengarten, R. A. Taylor, Nanofluid-based direct absorption solar collector, Journal of Renewable and Sustainable Energy 2 (2010) 033102.

[2] M. Karami, M. Akhavan-Bahabadi, S.Delfani, M.Raisee, Experimental investigation of CuO nanofluid-based direct absorption solar collector for residential applications, Renewable and Sustainable Energy Reviews 52 (2015) 793–801.

[3] R. Taylor, P. Phelan, T. Otanicar, R. Adrian, R. S. Prasher, Nanofluid optical property characterization: Towards efficient direct absorption solar collectors, Nanoscale Research Letters 6 (2011) 1931–7573.

[4] G. Ni, N. Miljkovic, H. Ghasemi, X. Huang, S. V. Boriskina, C.-T. Lin, J. Wang, Y. Xu, M. M. Rahman, T. J. Zhang, G. Chen, Volumetric solar heating of nanofluids for direct vapor generation, Nano Energy 17 (2015) 290–301.

[5] O. Neumann, A. S. Urban, J. Day, S. Lal, P. Nordlander, N. J. Halas, Solar vapor generation enabled by nanoparticles, ACS Nano 7 (2013) 42–49.

[6] O. Neumann, C. Feronti, A. D. Neumann, A. Dong, K. Schell, B. Lu, E. Kim, M. Quinn, S. Thompson, N. Grady, P. Nordlander, M. Oden, N. J. Halas, Compact solar autoclave based on steam generation using broadband light-harvesting nanoparticles, PNAS 110 (2013) 11677–11681.

[7] O. Neumann, A. D. Neumann, E. Silva, C. Ayala-Orozco, S. Tian, P. Nordlander, N. J. Halas, Nanoparticle-mediated, light-induced phase separations, Nano Letters 15 (2015) 7880–7885.

[8] O. Neumann, A. D. Neumann, S. Tian, C. Thibodeaux, S. Shubhankar, J. Müller, E. Silva, A. Alabastri, S. W. Bishnoi, P. Nordlander, N. J. Halas, Combining solar steam processing and solar distillation for fully off-grid production of cellulosic bioethanol, ACS Energy Letters 2 (2017) 8–13.

[9] A. Zeiny, H. Jin, G. Lin, P. Song, D. Wen, Solar evaporation via nanofluids: A comparative study, Renewable energy 122 (2018) 443–454.

[10] H. Jin, G. Lin, L. Bai, A. Zeiny, D. Wen, Steam generation in a nanoparticle-based solar receiver, Nano Energy 28 (2016) 397–406.

[11] M. Matsumoto, Surface Tension and Stability of a Nanobubble in Water: Molecular Simulation, Journal of Fluid Science and Technology 3 (2008) 922–929.

[12] X. Wang, Y. He, G. Cheng, L. Shi, X. Liu, J. Zhu, Direct vapor generation through localized solar heating via carbon-nanotube nanofluid, Energy Conversion and Management 130 (2016) 176–183.

[13] M. M. Rahman, H. Younes, G. Ni, J. Y. Lu, A. Raza, T. J. Zhang, N. X. Fang, A. Al Ghaferi, Plasmonic nanofluids enhanced solar thermal transfer liquid, AIP Conference proceedings 1850 (2017) 110013.

[14] X. Wang, Y. He, X. Liu, L. Shi, J. Zhu, Investigation of photothermal heating enabled by plasmonic nanofluids for direct solar steam generation, Solar Energy 157 (2017) 35–46.
[15] Y. Fu, T. Mei, G. Wang, A. Guo, G. Dai, S. Wang, J. Wang, J. Li, X. Wang, Investigation on enhancing effects of Au nanoparticles on solar steam generation in graphene oxide nanofluids, Applied Thermal Engineering 114 (2017) 961–968.
[16] A. Guo, Y. Fu, G. Wang, X. Wang, Diameter effect of gold nanoparticles on photothermal conversion for solar steam generation, RCS Advances 7 (2017) 4815–4824.
[17] H. Li, Y. He, Z. Liu, Y. Huang, B. Jiang, Synchronous steam generation and heat collection in a broadband Ag@TiO2 coreshell nanoparticle-based receiver, Applied Thermal Engineering 121 (2017) 617–627.
[18] G. Ni, G. Li, S. V. Boriskina, H. Li, W. Yang, T. Zhang, G. Chen, Steam generation under one sun enabled by a floating structure with thermal concentration, Nature Energy 1 (2016) 16126.
[19] H. Ghasemi, G. Ni, A. M. Marconnet, J. Loomis, S. Yerci, N. Miljkovic, G. Chen, Solar steam generation by heat localization, Nature Communications 5 (2014) 4449.
[20] S. Shin, J. T. Ault, P. B. Warren, H. A. Stone, Accumulation of Colloidal Particles in Flow Junctions Induced by Fluid Flow and Diffusiophoresis, Physical Review X 7 (2017) 041038.
[21] B. Faure, G. Salazar-Alvarez, L. Bergström, Hamaker constants of iron oxide nanoparticles, Langmuir 27 (2011) 8659–8664.
[22] E. T. Ulset, Utilizing Solar Vapour Energy by Use of Nanofluids in a Direct Absorption Solar Collector. Master Thesis, the University of Bergen., 2018.
[23] OSRAM, personal communication (email), additional informationon on the lamps (2017).
[24] B. V. Balakin, M. I. Delov, A. Kosinska, K. V. Kutsenko, A. A. Lavrukhin, Heat transfer during transition to nucleate boiling, International Journal of Heat and Mass Transfer 91 (2015) 1101–1105.
[25] M. Amjad, G. Raza, Y. Xin, S. Pervaiz, J. Xu, X. Du, D. Wen, Volumetric solar heating and steam generation via gold nanofluids, Applied Energy 206 (2017) 393–400.
[26] W. J. Minkowycz, E. M. Sparrow, J. P. Abraham, Nanoparticle heat transfer and fluid flow, CRC Press, 2013.
[27] C. Liu, J. Huang, C. Hsiung, Y. Tian, J. Wang, Y. Han, A. Fratalocchi, High-performance large-scale solar steam generation with nanolayers of reusable biomimetic nanoparticles, Advanced Science News 1 (2017) 1600013.
[28] S. V. Boriskina, personal communication (email), additional information on Ni et al. (2017).
[29] Y. Saint-Hilaire, R. Saint-Hilaire, Quasiturbine. http://quasiturbine.promci.qc.ca (2018).
[30] J. N. Israelachvili, Intermolecular and surface forces. Third Edition, Academic Press, 2011.
[31] C. Crowe, J. Schwarzkopf, M. Sommerfeld, Y. Tsuji, Multiphase flows with droplets and particles. Second Edition, CRC Press, 2012.
[32] G. De Falco, M. Commodo, P. Minutolo, A. D 'Anna, Flame-formed carbon nanoparticles: morphology, interaction forces, and Hamaker constant from AFM, Aerosol Science and Technology 49 (2015) 281–289.
[33] B. B. Mikic, W. M. Rohsenow, P. Griffith, On bubble growth rates, International Journal of Heat and Mass Transfer 13 (1970) 657–666.
[34] I. S. Tolubinski, Boiling heat transfer (in Russian), Kiev, Naukova Dumka, 1980.
[35] M. Liberman, N. Kleeorin, I. Rogachevskii, N. E. L. Haugen, Mechanism of unconfined dust explosions: Turbulent clustering radiation-induced ignition, Physical Review E 95 (2017) 051101.
[36] M. Dietzel, D. Poulikakos, On vapor bubble formation around heated nanoparticles in liquids, International Journal of Heat and Mass Transfer 50 (2007) 2246–2259.
[37] C. S. S. R. Kumar, Raman Spectroscopy for Nanomaterials Characterization, Vol. 1, Springer Berlin Heidelberg, 2012.

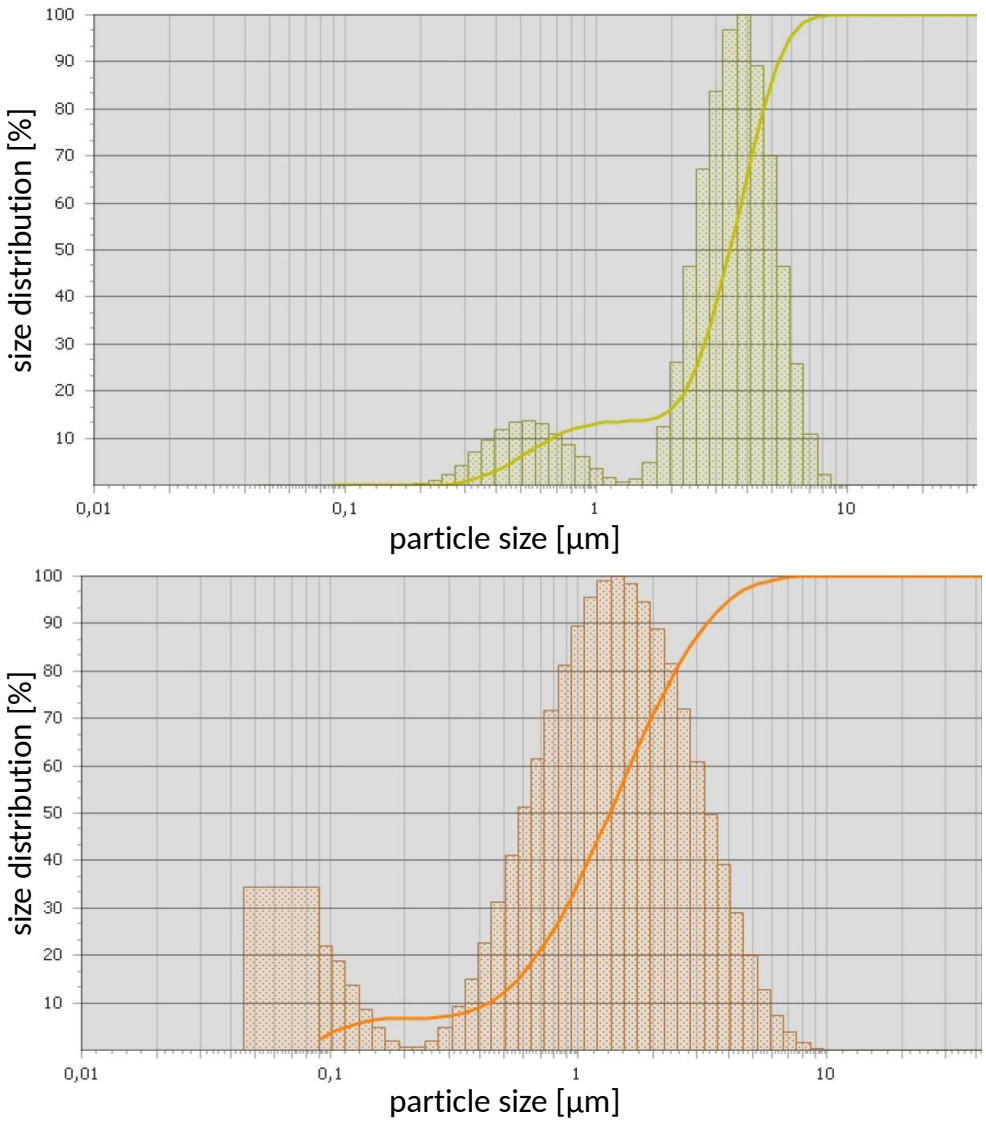

Figure 10: Particle size distribution in condensate samples from CBNF (top) and IONF (bottom).